ACS NANO

www.acsnano.org

ARTICLE

3D Nanoscale Structures of Hydrated Polyamide Desalination Membranes Revealed by Cryogenic Transmission Electron Microscopy Tomography

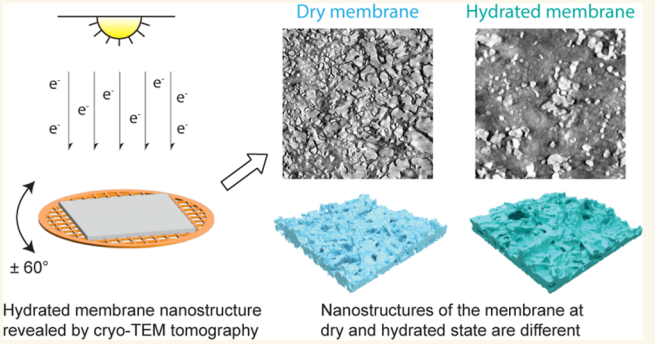
Chenhao Yao,[¶] Adi M. Ben-Zvi,[*,¶] Ruizhe Xu, Noa Ram, Mikhail Stolov, Priyanshu Gupta, Matthew J. Coupin, Harekrushna Behera, Viatcheslav Freger, Jamie Warner, Guy Z. Ramon, Manish Kumar,[*] and Tamar Segal-Peretz[*]

Cite This: *ACS Nano* 2025, 19, 16718−16731

Read Online

ACCESS | Metrics & More | Article Recommendations | Supporting Information

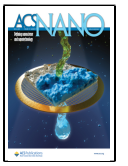
ABSTRACT: Desalination via reverse osmosis (RO) membrane technology is a preferred solution to the ongoing global challenges of freshwater scarcity. The active separation layer of RO membranes is a polyamide thin film (<200 nm), whose morphology critically influences membrane performance. However, conflicting descriptions of trends between morphology and performance abound in the literature due to the lack of a rigorous morphological description of these membranes. Notably, comprehensive three-dimensional (3D) morphological characterization of these membranes has so far been conducted exclusively under dry conditions, which contrasts with the operational, hydrated state of these membranes. Here, we present, for the first time, characterization of the hydrated 3D nanoscale morphology of polyamide films from commercial brackish water (BW) and seawater (SW) membranes using cryo-transmission electron microscopy (cryo-TEM) tomography. Our findings reveal significant morphological differences between hydrated and dry membranes, resulting in variations in key structural parameters that impact performance. Both SW and BW membranes swell and increase in total volume and thickness upon hydration, with BW membranes exhibiting more pronounced swelling (32% vs 7% in volume and 35% vs 11% in effective thickness), primarily due to the lower degree of cross-linking of BW membranes. Additionally, while the surface area decreases upon hydration for both SW and BW membranes, indicating a smoothing of surface nodules and cavities, surface roughness remains unchanged, suggesting that current roughness measurement methods such as atomic force microscopy do not capture intrinsic morphological features. Overall, this study demonstrates the feasibility of employing cryo-TEM tomography techniques to characterize RO membrane morphology under operation relevant conditions, thus enabling a better linkage between membrane morphology and performance.



KEYWORDS: *cryo-TEM tomography, 3D nanostructure, hydrated membrane, polymer swelling, morphology*

Drinking water scarcity is a major global challenge. With escalating global demand for reliable supply of clean water, seawater (SW) and brackish water (BW) desalination as well as wastewater recycling have emerged as pivotal solutions.[1] At the forefront of these advanced desalination and water reuse technologies are reverse osmosis (RO) membrane processes that have outstanding performance (>99% salt removal), relatively low operation costs, and high energy efficiency when compared to traditional thermally driven technologies.[1−6] Additionally, these membranes exhibit promising potential for applications in organic solvent filtration and gas separations.[1,5,7−10] Despite significant advancements in RO

Received: January 19, 2025
Revised: March 18, 2025
Accepted: March 19, 2025
Published: April 2, 2025



Downloaded via TECHNION-ISRAEL INST OF TECHNOLOGY on December 2, 2025 at 06:48:15 (UTC).
See https://pubs.acs.org/sharingguidelines for options on how to legitimately share published articles.

© 2025 American Chemical Society

https://doi.org/10.1021/acsnano.5c01190
ACS Nano 2025, 19, 16718−16731

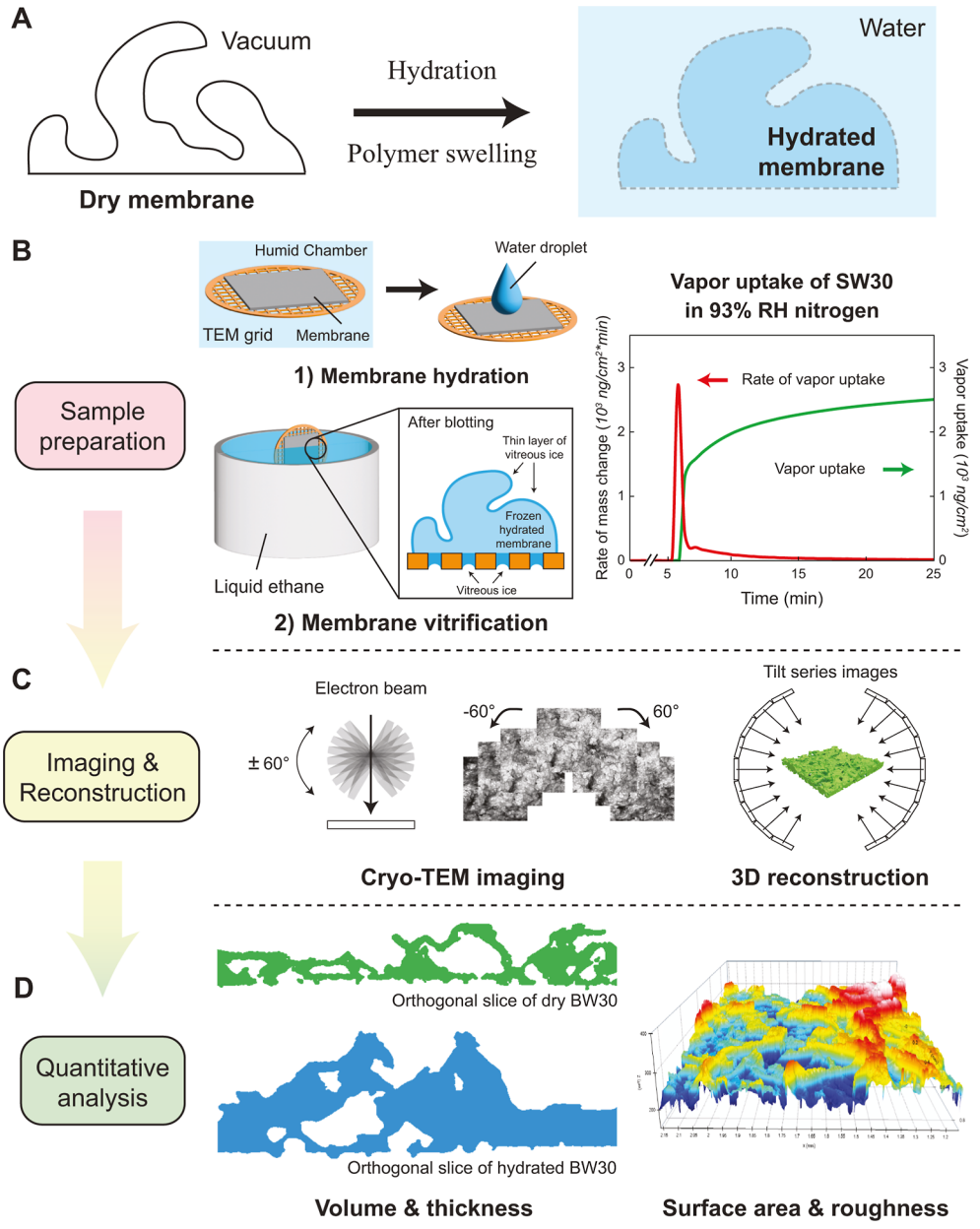


Figure 1. Cryo-TEM tomography and quantitative analysis of the 3D nanostructures can reveal details of the membrane nanoscale structure in the hydrated (close-to-functional) state and highlight differences from the dry state. (A) Characterization of dry membranes may not yield application-relevant membrane structures since the polymer network sorbs water during the filtration processes and this results in structural changes. (B) The general workflow of cryo-TEM tomography included hydration of the polyamide film with water vapor, wetting the surface with liquid water, blotting to remove excess water, followed by vitrification of the film by plunge freezing the sample in liquid ethane (vitrification) to preserve its hydrated structure. Equilibrium hydration was confirmed with water uptake measurement by QCM. (C) The 3D nanostructures were obtained from cryo-TEM tilt series acquisition and tomographic reconstruction. (D) Quantitative analysis of membrane properties such as membrane volume and thickness and surface area and roughness was conducted on the reconstructed 3D nanostructures.

membrane performance since their invention in the 1980s,[11] much of the progress has been achieved through an empirical, "Edisonian" approach.[12] Deciphering the factors that govern their performance, particularly synthesis conditions and the resulting nanoscale film morphology, remains an ongoing challenge.

The common structure of modern RO membranes is a thin-film composite (TFC), where a thin (<200 nm) polyamide film forms the active separation layer on top of a thick (>30 μm) porous polymer layer and a fabric support layer.[11] These polyamide films are typically fabricated via a rapid, exothermic interfacial polymerization reaction.[13,14] Polyamide film morphology strongly affects the resulting membrane permeability and water over salt selectivity,[15−22] but contradictory trends are often reported, primarily due to lack of a rigorous morphological description.[23−28] The complex morphology of the thin film 3D nanostructure has been commonly represented using various mean descriptors, including surface area, roughness, thickness, and polymer density, that are not sufficient for predicting performance. To characterize the heterogeneous film nanostructure in more detail and to better link it to membrane performance, advanced 3D quantitative characterization techniques using electron-microscopy tomography (ET) have recently been applied,[29−37] providing profound insights into the

https://doi.org/10.1021/acsnano.5c01190
ACS Nano 2025, 19, 16718−16731

morphology. For example, Culp et al.[31] contradicted reports that within the polyamide structure, there is a significant fraction of unconnected spaces (~30%), "enclosed voids", that may have a direct effect on membrane performance.[17] By using ET, they found that enclosed void fractions were less than 0.15% in SW and BW membranes, and thus, their impact on performance can be neglected. They also showed that ET is more accurate for surface analysis than the commonly used atomic force microscopy (AFM) technique. In a more recent study, Culp et al.[29] obtained 3D density maps of polyamide films, enabling linkage of the local polymer density distribution to water transport. However, to date, this thorough morphological characterization has been conducted exclusively under dry conditions, which fails to represent the true operational state of the desalination membrane, which is hydrated.

Polyamide hydration can significantly affect its structure. AFM studies have shown that hydration of SW and BW polyamide membranes led to ~10% and ~20% increase in their average thickness, respectively.[38,39] Lin et al.[17] reported that when SW and BW membranes were exposed to humidified nitrogen, their mass was increased by ~10%, as measured by quartz crystal microbalance (QCM), and Lee et al.[40] reported mass increases of ~20% in SW membranes using a gravimetric sorption analyzer. Kłosowski et al.[34] suggested various swelling mechanisms of polyamide, while Zhang et al.[41] used molecular dynamics (MD) simulations to study its swelling behavior. The latter study showed that a thicker polyamide film is more resistant to swelling due to a larger middle layer, which they define as a confined layer, that sorbs less water, while the top and bottom parts of the polyamide are the swelling layers, containing 90% of the bulk water density.[41] The hydration and swelling affect the membranes' permeability and selectivity as water-filled free volumes between the polymer chains act as transient and, in some cases, continuous pathways for small solutes and water molecules.[42] Therefore, to effectively correlate morphology with performance, it is essential to characterize the hydrated membrane structure using precise techniques. For this purpose, here, we describe the use of cryogenic transmission electron microscopy (cryo-TEM) tomography to reveal the 3D nanostructures of hydrated, swelled membranes and the differences in their structure from those of commonly characterized dry membranes.

In recent years, cryo-TEM tomography has revolutionized scientists' ability to probe complex 3D nanostructures in their native, aqueous environment. It has enabled detailed visualization of 3D systems such as whole organelles within cells, intricate cellular machinery, and bacterium−cell interactions, driving significant advancements in biological sciences.[43−45] Recently, the application of cryo-TEM tomography for synthetic materials has been explored,[46,47] where it emerged to be an effective tool for characterizing polymer morphologies, allowing researchers to decipher intricate polymer nano- and microstructures in solution.[48] Despite challenges such as sample sensitivity to the electron beam, low contrast between vitreous ice and polymer due to minimal density differences, and beam-induced motion, recent development in both hardware and software now enables better polymer visualization under cryogenic conditions.[31] These developments include the use of low dose imaging and direct electron detectors to minimize radiation damage, the use of energy filters, phase plates, and defocusing for contrast enhancement, and improved software for alignment and drift correction.[46] For example, recent work utilized cryo-TEM tomography for visualizing the morphological changes of lab-cast ultrathin polymeric electrolyte membranes upon hydration.[49−51] However, despite the advantages of cryo-TEM in numerous research fields, desalination membranes (commercial or lab-cast) have not yet been explored using this powerful technique.[48] Cryo-TEM tomography has the potential to visualize the close-to-functional hydrated morphology of desalination membranes, a crucial step for truly linking the membrane's morphology to performance.

In this work, we demonstrated the use of cryo-TEM tomography to achieve unprecedented visualization of the 3D nanostructures of commercial BW and SW polyamide desalination membranes in their hydrated states (Figure 1). This approach revealed significant morphological differences between hydrated and dry membranes and distinct swelling behaviors in BW and SW membranes, as discussed subsequently.

RESULTS AND DISCUSSION

Membrane Isolation, Hydration, and Vitrification. We isolated polyamide selective layers of commercial RO membranes (SW30 and BW30) from their backing layers by dissolving the polymer support in dichloromethane (DCM), following procedures described previously.[52] To minimize the possible collapse of the membrane structure during the isolation process, we compressed the membranes in a cross-flow filtration system prior to isolation in accordance with previous studies.[31] Due to the incompatibility between water and DCM, the compressed membranes were air-dried to remove residual solvent, and the isolated polyamide films were then rehydrated. Unlike biological samples, where cells and proteins are embedded within a layer of water, which can be thinned by blotting, the hydration of polyamide membranes for cryoimaging is restricted by their thickness. Polyamide films are typically 150−200 nm thick; thus, hydration by immersion in water results in water accumulation on the surface and the formation of vitrified ice, which is too thick for TEM imaging. To prevent this, we rehydrated the isolated and air-dried films in a humid chamber at 93% relative humidity (RH) for 24 h, followed by surface wetting with 10 μL of water for 10 min (Figure 1B). To confirm that the membranes reached equilibrium within the time scale of hydration, we performed microgravimetric measurements using QCM and measured the water uptake of the membranes upon exposure to humid nitrogen (~93% RH) and water (see Supporting Information for the detailed methods). Equilibrium was defined as the time point when the rate of mass increase reached 3 orders of magnitude lower than the initial rate after exposure, with a constant value less than 10 ng/cm^2 per minute, similarly to the benchmark previously reported by Lin et al.[17] Figure 1B shows a representative water uptake curve measured for the SW membrane in humid nitrogen. Significant water uptake occurred within the first minute of exposure, and the rate of mass change (red curve, which shows the slope of the green curve) increased by 3 orders of magnitude. Equilibrium was achieved, on average, within 23 and 30 min for SW and BW membranes, respectively (Figures 1B and S2). This is evident from the plateauing of the areal mass uptake and the rate of mass change decrease (Figure 1B). Upon exposure to degassed ultrapure water, SW and BW membranes reached equilibrium after 7 and 8 min, respectively. The water sorption analyses thus indicate that the exposure time in our protocol was sufficient to fully hydrate the RO membranes at ~93% RH and in pure water. Membrane hydration was also validated by observing vapor/hydrogen bubble formation, caused by water radiolysis by the electron beam during cryo-

https://doi.org/10.1021/acsnano.5c01190
ACS Nano 2025, 19, 16718−16731

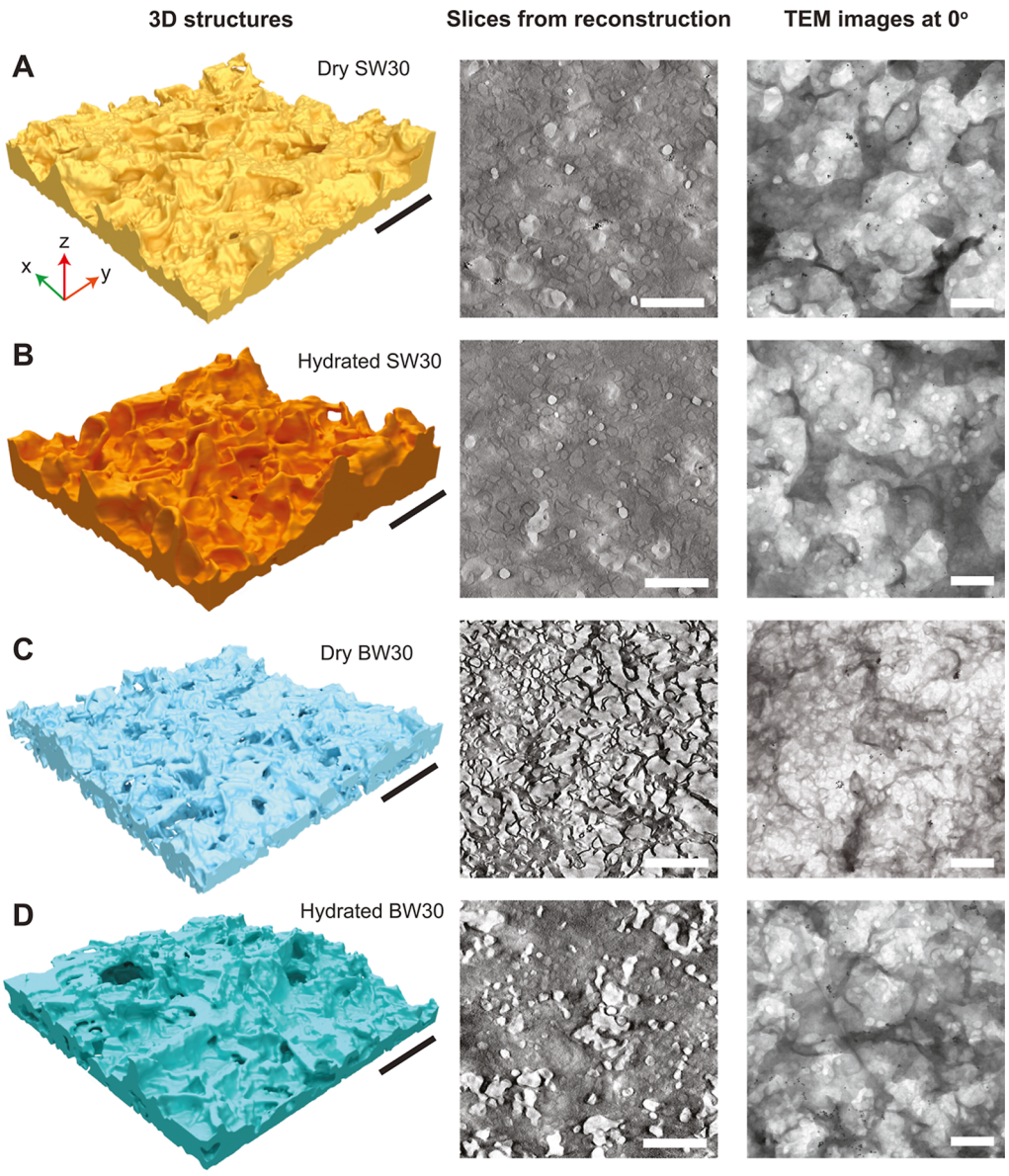


Figure 2. Reconstructions and 3D models revealed differences in the nanostructures of dry and hydrated SW30/BW30 membranes, which were not discernible in 2D TEM images. Left column: Reconstructed 3D nanostructures of the membranes showed ridge-and-valley morphology on the surface and quantitatively showed the difference in degrees of swelling between SW30 and BW30 membranes. Middle column: Representative slices from the reconstructed tomograms highlight differences between membranes in their dry and hydrated states: both SW30 and BW30 exhibited changes in surface morphology after hydration (B,D vs A,C); BW30 showed a greater degree of swelling indicated by the transition from a "open" structure in the dry state (C) to a less "open" structure after hydration (D). Right column: The pixel intensity (electron intensity) in TEM images taken in a bright-field mode at 0° tilt angle provided limited information about membrane nanostructures, except for indication of the overall amount of material. Scale: 500 nm.

TEM imaging of hydrated samples subjected to deliberate high-dose conditions.[53] This phenomenon was not observed in dry samples (Figure S6 and Supporting Information Movies S1 and S2).

Prior to vitrification, a blotting process was performed in a plunge freeze (Vitrobot) instrument to remove the excess water from the membrane surface and enable sufficient contrast in the cryo-TEM imaging. The blotting time was carefully set to remove as much surface water so that a very thin ice layer would cover the membrane surface after vitrification while minimizing the removal of water sorbed in the polymer network (Figure 1B, see Supporting Information for details). The hydrated membrane structure was then preserved by plunge-freezing the sample in liquid ethane (Figure 1B). At this high cooling rate, water sorbed in the polymer network and on the membrane's surface is vitrified, i.e., it is transformed into an amorphous, glassy state that is electron-transparent and does not damage the hydrated structures with phase change.[54,55] This is in contrast to conventional freezing, where electron-scattering crystalline ice is formed and structural damage can occur due to ice nucleation and crystallization. The vitrification process ensures that the hydrated state of the membranes and its structure are maintained and can be imaged under the high-vacuum conditions of the microscope. To investigate the effect of hydration on the membranes' structure while accounting for structural changes that might be caused by sample preparation, both dry and hydrated membranes went through the same

https://doi.org/10.1021/acsnano.5c01190
ACS Nano 2025, 19, 16718−16731

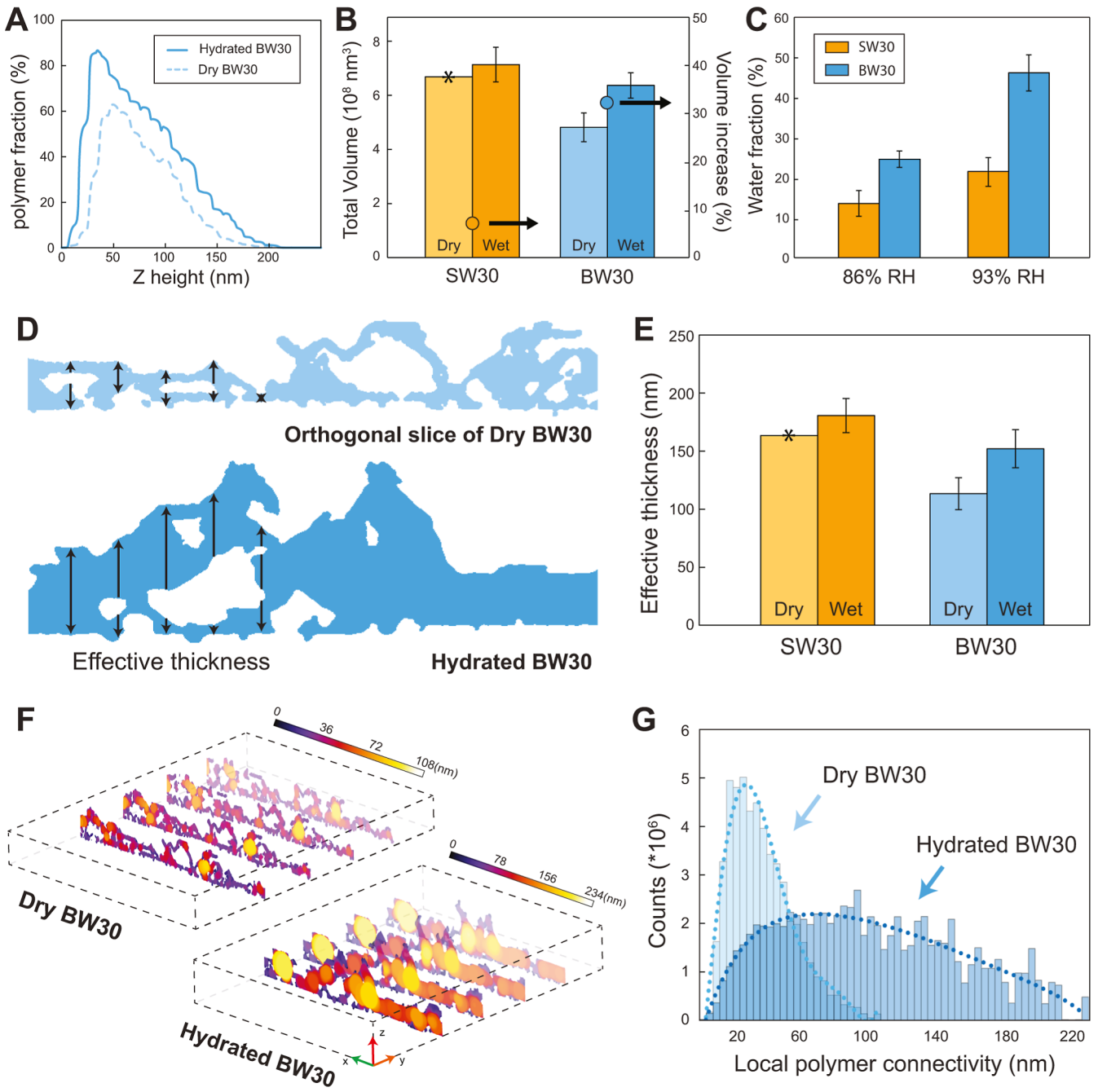


Figure 3. Quantitative analysis on reconstructed models indicated that SW30 is generally thicker than BW30 in both dry and hydrated states, while BW30 showed more significant swelling than SW30 under the same hydration conditions. (A) Polymer fraction per horizontal slice, and (B) the total membrane volume was calculated for each membrane, and the increase after hydration can be clearly seen. BW30 showed greater increase in volume (32% vs 7%) than SW30 after hydration. (C) Equilibrium water uptake measured by QCM agrees with the observed volume increase, where BW30 showed a greater water fraction (45% vs 22%) than SW30 after equilibration with 93% RH nitrogen. (D) Effective thickness was calculated to more accurately represent the thickness of membrane materials by excluding the nonpolymer pixels. (E) BW30 showed a greater increase in effective thickness than SW30 (35% vs 11%), which agrees with the trend in the total volume increase. (F) The local polymer connectivity of the membranes was calculated to evaluate the change in material distribution after hydration. Different slices (distance in between: 20 nm) of the 3D structures are presented to show the change in the local polymer connectivity at different positions within the membranes. (G) BW30 showed a broader distribution of local polymer connectivity and a higher maximum value after hydration (232 nm vs 108 nm), indicating that the structure in dry BW30 became less "open" while the voids were filled with swollen polymer. The error bars represent one standard deviation among three samples of each membrane type. *: only two reliable samples were analyzed and only the average values were reported for dry SW30.

plunge freezing and blotting cycle and were imaged under the same conditions.

Imaging and 3D Reconstruction of Dry and Hydrated RO Membranes. 2D TEM images of both dry and hydrated RO membranes at different tilt angles were acquired with a 300 kV Titan Krios G3 cryo-electron transmission electron microscope. The tilt series was acquired from −60 to 60° in 1° increments, and a low electron dose rate (~0.22 $e^-/Å^2/s$) was

https://doi.org/10.1021/acsnano.5c01190
ACS Nano 2025, 19, 16718−16731

used to minimize sublimation of vitreous ice and beam radiation damage. Due to the relatively low signal-to-noise ratio in cryo-TEM imaging, the raw tilt series images and reconstructions had low contrast (Figures S7 and S8);[56,57] therefore, a linear contrast stretching was performed to enhance the image contrast for segmentation.[58] The right column in Figure 2 shows representative TEM images of dry/hydrated SW30 and BW30 membranes taken at 0°. The pixel intensity, or visual brightness, of the image of dry BW30 is higher than the other three membranes, indicating that there was less scattering of electrons caused by interaction with the membrane and potentially less material (polymer or ice) in dry BW30.[59] Despite this qualitative observation, limited information about the 3D nanostructure can be extracted from the 2D images as both the surface and internal features of the membranes are superposed in these projection images. To reveal more information about the nanostructure of the membranes, 3D reconstructions were performed using the acquired tilt series.

Membrane nanostructure reconstructions were performed using the filtered back projection (FBP) algorithm in IMOD.[60] For each sample type, 5−10 tilt series were recorded, and from these, 2−3 tilt series that exhibited the highest contrast and minimal contamination were reconstructed into tomograms. The tomograms of the same membrane type showed high similarity (Figure S8). Representative tomograms are shown in Figure 2. Due to the missing-wedge effect,[61,62] streaking artifacts were observed in all the constructed models and a combination of thresholding and manual correction was used during segmentation to minimize the errors caused by such artifacts (Figure S9). As expected, the well-known, characteristic ridge-and-valley surface morphology of polyamide TFC RO membranes[63] was observed in all the reconstructed models as shown in the left column of Figure 2. Compared with the rough top surfaces, the bottom surfaces of the membranes at the polyamide−polysulfone interface were generally smoother (Figure S10). This observation is also consistent with other reported tomographic studies of dry polyamide RO membranes.[29,33,64] Our reconstructed 3D nanostructures, however, indicated significantly different swelling behaviors between SW and BW membranes: the change in morphology for BW membranes was more evident than for SW membranes under the same hydration conditions. The middle column of Figure 2 shows representative horizontal slices of the reconstructed tomograms (for each membrane, the slice with the highest polymer fraction is shown), and striking differences between the membranes can be seen. As also shown in orthogonal slices (Figure S11) of the 3D nanostructures, dry BW membranes appear to have more open spaces than dry SW membranes. However, while the structure of SW membranes remained almost unchanged after hydration, BW membranes showed significantly reduced "openness" (Figures 2C,D and S11C,D). SW membranes have higher rejection for dissolved species but lower water permeability compared to BW membranes, a performance difference attributed to the higher degree of polyamide cross-linking in SW membranes.[65−67] This increased cross-linking also accounts for the observed differences in swelling,[68] as will be discussed in more details in the following sections. Quantitative analyses were performed on all segmented 3D reconstructions to compare the nanostructures of dry and hydrated RO membranes and evaluate the differences in their swelling characteristics. Properties that are relevant to water transport, such as thickness and accessible surface area, were also calculated and compared between the different samples.

Membrane Volume and Thickness. Membrane volume was calculated as the sum of voxels categorized as a dry or swollen (hydrated) polymer in the 3D nanostructures. This metric allows us to directly probe the volume differences that arise from membrane hydration and compare different membrane samples. By analyzing each $x-y$ slice (2 nm thick) along the z axis, the polymer areal fraction was calculated as a function of z height (membrane thickness), where the first and last slices containing polymer pixels were defined as the bottom (z = 0 nm) and top of the membrane, respectively. Figures 3A and S12 show the polymer fraction profile of dry and hydrated BW30/SW30 membranes. The total volume of BW30 increased significantly after hydration, as indicated by the higher polymer fraction in each slice along the z-axis. Although this increase in volume indicated that the total amount of materials (i.e., polymer and ice) of BW30 increased after hydration, the actual polymer content of the membranes remained the same and the increase was mainly a result of polymer swelling caused by water sorption. In contrast to BW30, the SW30 membrane did not show significant changes after hydration. Analysis of the total membranes volume (Figure 3B) indicates that upon hydration, BW30 had a larger increase in volume from $4.88(\pm0.54) \times 10^8$ to $6.45(\pm0.47) \times 10^8$ nm^3 (~32%) compared to SW30 (~6.8%) (Table S1). This difference can also be observed in the respective horizontal slices: for dry BW30, most of the slices show large open areas (Figure 2C) that seem to disappear after hydration (Figure 2D). We propose that this "void closure" is likely due to expansion of the polymer after water uptake, reminiscent of polymer hydrogels. SW30, on the other hand, did not show a significant difference between dry and hydrated states, indicating that the polymer did not expand as considerably as in BW30. The classic model that relates polymer swelling to its molecular structure is the Flory−Rehner theory,[69] which describes the thermodynamics of polymer swelling as a balance between the free energy of mixing between a polymer and a solvent and the elastic energy associated with the polymer chain stretching. Studies have also identified the limitations of applying the Flory−Rehner theory to polyamide membranes (e.g., the assumption of affine swelling and improbable 3D swelling in thin 2D films) and proposed improved models such as the Painter−Shenoy to more accurately describe the swelling behavior of polymeric systems (see Supporting Information for equations and additional discussion).[70−74] In these theories, the swelling ratio (S) of the polymer at a certain solvent activity was mainly scaled to two properties of the polymer network: the number of monomer units between two cross-link sites (N) and the Flory−Huggins interaction parameter between the polymer and the solvent (χ) (Table S2). In general, when all other parameters (network functionality (f) and packing factor (P)) are equal, polymers with a lower degree of cross-linking (larger N) and favorable interaction with the solvent (smaller χ) will have a greater degree of swelling. In this study, the lower degree of cross-linking (smaller N) in BW30 compared to SW30 is proposed as the main reason for the different swelling ratios measured from the tomography data. Studies have also shown that the interaction parameter χ scales linearly with cross-linking density,[75] thus, these two parameters have a synergistic effect on the swelling ratio of less cross-linked polyamide membranes.

The lower degree of cross-linking of the BW30 membrane was also confirmed with the water uptake measurements by QCM. Figure 3C shows the water fraction (see explanation in Supporting Information, QCM analysis section) after the membranes reached equilibrium upon exposure to humid

https://doi.org/10.1021/acsnano.5c01190
ACS Nano 2025, 19, 16718−16731

nitrogen at 86% and 93% RH. The water uptake by BW30 was 12.4% and 21.8% at 86% and 93% RH, respectively, which was ∼2 times higher than that of SW30 (7.6% and 10.1%). The increased water uptake at higher RH (i.e., water activity) is consistent with the observation reported by Lee et al.,[40] and the difference between BW30 and SW30 matches the trend in their total volume (Figure 3B).

To further understand the relationship between the membranes' 3D nanostructures and their swelling characteristics, we calculated the thickness of the "confined" layer,[41] which is also referred to as a low-void-fraction layer, by measuring the distance between two horizontal slices containing at least 85% membrane material.[33] The "confined" layers of all membranes analyzed in this study were found to be closer to the bottom side of the membrane, and their thicknesses were measured to be 60/82 and 0/13 nm for dry/hydrated SW and BW membranes, respectively (Table S1). We found that the "confined" layer in SW30 was much thicker than that in BW30, in agreement with Zhang et al.'s[41] observation by MD simulations that a thicker middle layer tends to sorb less water. It is also worth noting that there was no low-void-fraction layer in dry BW30, indicating that the structure was relatively "open". After hydration, the low-void-fraction layer thickness was increased to 13 nm, indicating that the polymer swelled and expanded laterally as well as vertically to fill the "open" areas. The lateral expansion of the polymer can be clearly observed in Figure 3A, as the polymer fraction of each slice in the hydrated BW30 nanostructure is higher than that of dry BW30. This 3D expansion is in contrast to the 1D expansion proposed in other studies,[70−73] where the thin polyamide films were considered laterally confined or laterally infinite and the material could stretch and expand in only one direction (i.e., away from the support with only a change in thickness). This contradictory observation implies that for membranes with more uniform and less open structures that were previously studied (e.g., NF-type,[70] model mLBL,[71] and SWRO-type membranes[72]), the polymer chains were restricted from stretching laterally, leading to swelling primarily in the vertical direction. As a result, modified 1D swelling models were applicable. However, in the current case where membranes with a more open structure are present (i.e., BWRO-type membranes), the polymer chains are less constricted and can expand laterally to fill the internal voids. As suggested by Orski et al.,[76] thermodynamic models need to be critically examined when there is a discrepancy between the data (i.e., thickness) obtained from commonly used spectroscopy techniques (e.g., X-ray reflectivity) and real-space images/structures from microscopy. We propose that 3D characterization using TEM and cryo-TEM tomography provides a more accurate basis for developing comprehensive models and better understanding of the structure−property-performance relationship in polyamide RO membranes.

The difference in the membranes' ability to sorb water and swell was also validated from thickness calculations. Membrane thickness is conventionally measured using ellipsometry and from SEM/TEM images of membrane cross sections.[77,78] These measurements do not necessarily yield accurate and representative values. For example, in ellipsometry, the thickness is measured by averaging the signal originating from the beam area (usually millimeters in diameter), which may not fully capture the thickness variation of the membrane's surface. This might lead to inaccurate estimation of the actual thickness, particularly for RO membranes, which typically have a rough ridge-and-valley surface morphology. In cross-sectional imaging, point-to-point thickness measurements often include open areas within the membrane, which likely do not contribute to water transport or salt rejection. This can result in an overestimation of the actual thickness when modeling performance. In this study, we propose a new method to determine the effective thickness by considering only the polymer-containing voxels in the 3D nanostructures obtained from tomography. We averaged this measurement over the entire field of view to ensure reliable statistics. This tomography-based effective thickness excludes the effect of open or enclosed voids on the membrane thickness, providing a more accurate representation of the actual polymer material. Compared to cross-section analysis where only a limited number of point measurements can be made, this method is based on a large number of measurements, which provide statistical information on the thickness variation within the field of view. As illustrated in Figure 3D, the binary orthogonal slices were first produced by reslicing the 3D nanostructures along the y axis. From each z column in the orthogonal slices, only the membrane voxels were counted, and the counts of all columns (10^6 in a 2×2 μm field of view with 2 nm pixel size) within the measured area were averaged to obtain the effective thickness. The effective thickness of dry BW30 was measured to be 113 ± 14 nm, which is significantly lower than previous measurements by cross-section SEM, TEM, and AFM (∼150−180 nm).[79] The effective thickness of dry SW30 (163 ± 9 nm), on the other hand, is similar to the reported values (∼170 nm),[79] which is consistent with our observation of less open spaces in SW30 compared to BW30. After hydration, the effective thickness of BW membranes increased by 35% from 113 ± 14 to 152 ± 16 nm, while that of the SW membrane only increased by 11% from 163 ± 9 to 181 ± 15 nm (Figure 3E).

To further evaluate changes in membrane morphology due to hydration, we calculated the local polymer connectivity of the membranes, which was also referred to as "local thickness" by Song et al. for polyamide membranes[36,64] and widely used in other applications of tomography.[80,81] In this method, the local polymer connectivity at each voxel is defined as the diameter of the largest sphere that can contain the voxel and remain inside the membrane material. This parameter describes how the polymer voxels in the 3D membranes nanostructures are connected (rather than a "thickness" which would imply the direction of water/solute transport), and while the effective thickness is an overall and averaged description of membrane thickness, the local polymer connectivity of the membranes provides information on the distribution of membrane materials and can potentially be a more descriptive characterization of local membrane volume expansion. This metric also provides insight into the path length of transmembrane permeation.[36] The visual rendering of this metric as spherical interconnected volumes is also an effective tool for conveying distribution of polymer within volume reconstructions. The orthogonal slices of dry and hydrated BW30 (Figure 3F and Supporting Information Movie S3) show a significant increase in local polymer connectivity after hydration, in good agreement with the trends seen in effective thickness and volume. This observation was also confirmed by the local polymer connectivity histogram shown in Figure 3G, where dry BW30 presents a unimodal distribution with a peak at 32 nm and a maximum connectivity of 108 nm, and hydrated BW30 shows a broader distribution with the maximum connectivity of 232 nm with a peak at 88 nm. Similar to total volume and effective thickness trends, the average local polymer connectivity of BW30 increased ∼3 times from 43 ± 3 to 116 ± 13 nm after

https://doi.org/10.1021/acsnano.5c01190
ACS Nano 2025, 19, 16718−16731

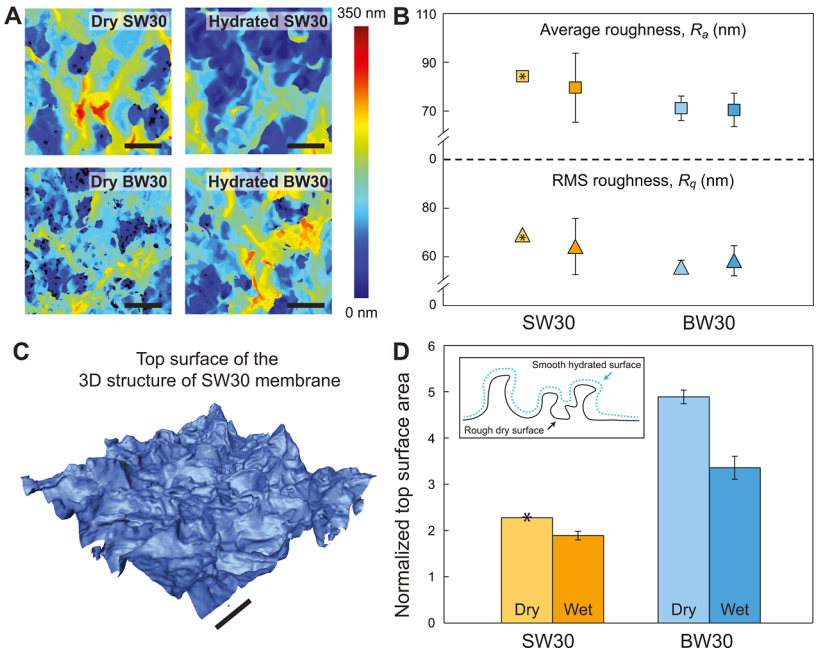


Figure 4. 3D membrane nanostructures allowed accurate analysis of surface roughness and accessible surface area. (A) Top views of the surface height map of the four membranes were generated in OmiSurf3D. (B) The average and rms roughness values of the top surface were calculated and no significant change was observed between dry and hydrated membranes. (C) The top surface that was isolated from the 3D nanostructures in Amira-Avizo software; this illustration shows the surface of the hydrated SW30 membrane. (D) Normalized surface area was calculated by dividing the area of the surface by the area of the field of view. Dry membranes generally showed greater normalized top surface area than hydrated membranes. Scale: 500 nm. The error bars represent one standard deviation among three samples of each membrane type. *: only two reliable samples were analyzed and only the average values were reported for dry SW30.

hydration, where that of SW30 only increased ~15% from 108 ± 8 to 125 ± 13 nm (Figure S13 and Table S1).

Overall, both SW and BW membranes swelled under the same hydration conditions, with BW membranes showing more pronounced swelling than SW membranes, as evident by the greater increase in total volume, effective thickness, and local polymer connectivity in BW membranes. These observations align with the reported lower degree of polyamide cross-linking of BW membranes compared to SW membranes.[65−67] This difference in cross-linking is consistent with the higher operating pressure and greater tolerance to high salinity feeds in SW membranes. Additionally, the higher thickness of SW membranes may also contribute to their higher salt rejection and lower water permeance compared to BW membranes.[24,67] In addition to the membrane volume and thickness, we also analyzed the enclosed void fraction content. Similar to our previous work,[31] we considered only the voids that are completely enclosed by membrane material (i.e., enclosed voids) (Figure S15). We found that the enclosed void fractions of dry and hydrated SW30/BW30 membranes are all below 0.5% (Table S3), in concurrence with our previous reports[31] and in marked contrast to earlier reports of higher values (~15−32%) calculated from water uptake.[17] We propose that this discrepancy arises mainly from the inclusion of open voids in other measurement techniques.[82,83] Given the very low enclosed void fraction observed in all the hydrated membranes' 3D nanostructures, the enclosed voids are likely to have negligible impact on membrane performance. This point was also made in a previous modeling study using simplified film geometry.[20] Specifically, it was shown how film roughness that corresponds to greater void volume has little impact on film permeance when the voids are enclosed, as the dominant transport resistance comes from the layer of polymer that separates the void from the permeate space. The model also clearly showed how, on the other hand, a clear positive correlation exists between roughness and permeance when the voids are connected to the permeate.[20] In this context, crumpled film features that are connected to the permeate represent favorable structures, whereas other roughness features (particularly when shown in 3D, to be connected with the feed) are merely structures that for the most part do not contribute to transport. Based on this insight and the results reported here, it is apparent that morphological analysis would be best if focused on bulk polymer properties and the permeate-connected surface morphologies of hydrated membranes.

Surface Roughness and Accessible Surface Area. The surface morphologies of SW30 and BW30 membranes are well-known for their crumpled, ridge-and-valley structures, which can significantly influence the water permeance and fouling resistance of the membranes. Previous studies have suggested that membranes with these crumpled surface structures could have increased accessible surface and effective filtration area, thus resulting in higher water permeance.[84] Other studies have also shown that the ridges and valleys on the membrane surface can potentially accumulate foulant during the filtration process,[85,86] which can reduce the membrane performance. However, the commonly used surface characterization techniques (i.e., AFM and SEM) were mostly performed on a dry membrane, whose structures, as previously discussed, are very different from their hydrated, functional states. In this study, we characterized the top surface morphology of both dry and hydrated SW30/BW30 membranes using the 3D nanostructures reconstructed from cryo-TEM tomographs to gain a more comprehensive understanding of how membrane swelling influences the surface roughness and surface area and assessed whether the commonly used characterization parameters can

https://doi.org/10.1021/acsnano.5c01190
ACS Nano 2025, 19, 16718−16731

reflect the difference between dry and hydrated membrane surface morphology.

The roughness of the RO membrane surface is typically characterized by average roughness (R_a) or root-mean-square roughness (R_q) and measured with AFM or profilometry.[42] Although these techniques allow the characterization of membranes in the hydrated state (i.e., liquid-state AFM), their accuracy is limited by the incomplete representation of the complex surface features due to the finite thickness of the AFM tip (Figure S16). The 3D nanostructures reconstructed from cryo-TEM tomography provide a more accurate way of measuring the membrane surface roughness. We computed surface height maps of both SW30 and BW30 at dry and hydrated states from their 3D structures (Figure 4A) and calculated their R_a and R_q values (Figure 4B). The R_a/R_q measured for dry SW30 and BW30 are 69.1 ± 1.1/84.3 ± 3.3 and 55.8 ± 2.8/71.1 ± 5.0 nm, respectively; these values are consistent with the reported values measured with AFM.[87] Interestingly, we did not observe any correlation between the increase in volume/thickness and the change in surface roughness. As shown in Figure 4B, there was very little change in both average and root-mean-square (rms) roughness of SW30 (<7%) and BW30 (<5%) after hydration. Despite the obvious change in the appearance of the membranes' surface and significant increase in volume and thickness, the roughness of the membranes remained relatively constant. This observation can be attributed to the change in the ridge-and-valley structures after hydration: when the "ridges" sorbed water and expanded laterally, the initial "valleys" became smaller, resulting in a flatter membrane surface. This analysis indicates that the roughness of RO membranes may not be fully captured by R_a and R_q values and that the 3D nanostructures obtained from cryo-TEM tomography could provide a more comprehensive understanding of how surface features change shape upon hydration through surface topology analysis (e.g., the shape of surface crumples[32] and curvatures of surface features[33]).

The reconstructed 3D nanostructures also allowed the calculation of the accessible surface area of the membranes. In previous reports,[31,33] the actual surface area of dry RO membranes was found to be ∼2−5 times greater than their projected surface area. Kalutantirige et al.[64] suggested that using the actual surface area led to better modeling and prediction of the membranes' water and solute transport properties. We used the Amira-Avizo 2023.1 software package to isolate the top surfaces from the 3D nanostructures of the membranes (Figures 4C and S17) and calculated the actual surface area and normalized surface area (see Supporting Information for details). The actual top surface area of the dry SW30 and BW30 was 2.27 ± 0.16 and 4.89 ± 0.15 times higher than their projected areas, respectively (Figure 4D). This finding is consistent with previous literature reports.[33] The normalized surface area of dry BW30 is ∼2 times higher than that of SW30, probably due to the greater number of ridges and valleys, as well as open voids on the membrane surface, as seen in Figure 2.

To further analyze the actual surface area of the membranes in their hydrated state, we also performed surface area calculations on the 3D nanostructures of hydrated SW30 and BW30. Interestingly, although the height and volume of the ridges on the membrane surface seemed to have increased by simple observation, the normalized surface area calculated actually decreased to 1.89 ± 0.09 and 3.35 ± 0.25 for SW30 and BW30, respectively (Figure 4D). Surface area can increase for several reasons: an increase in size, the presence of surface irregularities (i.e., pores, voids, or modules), changes in shape, and the division of a particle into smaller particles, creating new surfaces.[88] Kłosowski et al.[34] suggested different swelling mechanisms for polyamide membranes that involve internal and external expansion (i.e., ballooning and stretching). Thus, we propose that the reduction in surface area of both BW30 and SW30 after hydration can be attributed to the following morphological changes: expansion of the polymer structure due to swelling leads to an increase in volume and thickness; however, the rough surface features merged into larger features, smoothing out the irregularities and reducing the overall surface area (Figure 4D inset, Figure S18). In addition, the open voids on the surface decreased in size and disappeared upon union of the rough features. The decrease in surface area upon swelling of both membrane types demonstrates the importance of using cryo-TEM tomography to reveal the surface structures of hydrated membranes and using the surface areas of the hydrated rather than dry membranes as a parameter when developing the structure−performance relationship for polyamide RO membranes.

The distribution of polymer density across the membranes is also an important parameter in understanding the structure−performance relationship of polyamide RO membranes, as this distribution dictates the critical morphological features that impact water permeance.[31] Some studies suggested that regions with lower polymer density tend to have higher water flux, and such flux "hot spots" can potentially make the membranes more prone to fouling.[89] Culp et al.[31] used high-angle annular dark-field scanning TEM tomography to demonstrate that a dense polyamide layer in commercial dry BW and SW membranes is located at the top surface, directly affecting membrane performance. Looking into future research, obtaining 3D maps of the polymer density of hydrated membranes using techniques such as cryo-STEM tomography will be an important step for further understanding the behavior of these membranes in real, hydrated conditions.

CONCLUSIONS

In this work, we demonstrated that cryo-TEM tomography can resolve the structures of polyamide RO membranes in their hydrated (close-to-functional) state, which enabled quantitative analyses of changes in membrane morphology upon hydration. Although current methods for characterizing hydrated membranes such as liquid-state AFM and QCM provide valuable insight on membrane morphology and thickness, cryo-TEM tomography offers a more detailed, high-resolution, 3D characterization of hydrated membrane structures and therefore enables more accurate calculations of the membrane's characteristics.

The presented study of hydrated membranes employing cryo-TEM tomography is a significant step toward understanding functional RO membrane structures. Cryo-TEM tomography can provide accurate characterization of key properties such as thickness and surface area, which are central for studying water and solute transport across RO membranes. Future research should focus on adding advanced reconstruction algorithms and microscopy-spectroscopy techniques such as cryo-scanning transmission electron microscopy (cryo-STEM) and electron energy loss spectroscopy,[90] with which to better resolve the membrane structure and reveal additional properties such as polymer density distribution. Moreover, more realistic constraints (e.g., pressure applied on the top surface of the membrane) can be applied to the membrane hydration

https://doi.org/10.1021/acsnano.5c01190
ACS Nano 2025, 19, 16718−16731

procedure to gain more thorough understanding of confined membrane swelling,[91] or deswelling,[92] during the real filtration process where membranes are continuously compressed by the feed stream.

MATERIALS AND EXPERIMENTAL METHODS

Membrane Pressurization and Isolation. SW30HRLE and BW30XFRLE membranes (Dupont Water Solutions, Edina, MN) were received as dried flat sheet membranes. The membranes were compacted in a cross-flow filtration setup following previously published protocols.[31] Briefly, the membranes were operated in a crossflow cell with ultrapure water at 225 psi for 12 h at a flow rate of 5 L/min. The compacted membranes were taken out of the cross-flow cell and dried overnight at room temperature. To isolate the polyamide selective film, the dried TFC membranes were immersed in dichloromethane (DCM, >99.5%, purchased from VWR) to dissolve the middle polysulfone layer, leading to the detachment of the polyamide layers from the backing, which become free-floating. TEM grids (200 mesh copper, Ted Pella) were pretreated with UV−ozone to make the surface more hydrophilic and improve the compatibility with wet PA films. The free-floating PA films were transferred onto the pretreated TEM grids by directly picking them up from the DCM. The PA films on the grids were then thoroughly cleaned in fresh DCM to remove all residual polysulfone. The PA films were firmly attached to the grid and did not float off during the cleaning process.

Membrane Hydration and Vitrification. The isolated membranes on TEM grids were air-dried overnight to remove residual DCM. To deposit fiducial markers to aid future computational alignment of acquired images, 15 nm gold nanoparticles (OD1, stabilized in 0.1 M PBS) were purchased from Sigma-Aldrich. The gold nanoparticle suspension was diluted with 60% (volume) ethanol and then deposited on the membrane surface by spin coating 20 μL of the diluted solution. For dry samples, the membranes were stored at room temperature and in ambient air until the vitrification step. For hydrated samples, the coated membranes were placed in a custom-made humid chamber with ∼93% RH to allow overnight equilibration with vapor; 10 μL of pure water was added to the surface of hydrated membranes for 10 min in a 100% RH chamber to further hydrate the surface. Both dry (membranes without the humid chamber and surface wetting) and hydrated membranes were vitrified in liquid ethane by using a FEI Vitrobot Mk. IV, and the blotting condition was set to a blotting force of 0 and blotting time of 30 s. The blotting conditions were carefully chosen so that (1) most of the water on the membrane surface was removed which resulted in a very thin ice layer after vitrification; thus, the contrast in the TEM images was mostly from polymer and vacuum, and (2) the water absorbed inside the membrane was not removed by excessive blotting. Shorter blotting time (i.e., 20 s) resulted in a large area of the membrane covered in thick ice which could not be imaged under cryo-TEM and longer blotting time (i.e., 60 s) resulted in dried areas in the hydrated samples similar to the dry ones. The vitrified membranes were stored in liquid nitrogen until imaging.

Vapor Uptake Measurement by QCM. To ensure that the SW and BW membranes reached equilibrium hydration within the hydration time frame (overnight in 93% RH and 10 min of surface wetting by pure water) described above, we performed in situ microgravimetric measurements to measure the increase in mass of PA membranes over the hydration period. We tested three hydration conditions: 86% RH, 93% RH, and degassed Milli-Q water. For each test, we allowed the system to reach equilibrium, defined as a negligible constant mass increase over time $\left(<10\frac{\text{ng}}{\text{cm}^2\,\text{min}}\right)$, which is at least 3 orders of magnitude lower than the initial mass increase. Gold-plated QCM sensors (Renlux Crystal, 5.0 MHz resonant frequency) were prepared as previously described.[93] The sensors were cleaned using a UV−ozone chamber (ProCleaner, BioForce Nanosciences), followed by sonication in ethyl alcohol, rinsing with Milli-Q water, drying with nitrogen, and a final additional UV−ozone treatment. Detailed QCM measurements and analyses can be found in Section 1.1 in the Supporting Information.

Tilt Series Images Acquisition, Tomogram Reconstruction, and Segmentation. Membrane samples were screened before tilt series images acquisition to ensure integrity and lack of contamination so that there was a minimal amount of grid bending or contaminants that would affect image/reconstruction quality. 2D cryo-TEM images of the membrane samples were taken at 0° in a 200 kV Glacios cryo-TEM microscope (Thermo Fisher Scientific). Screening was performed at 28,000× magnification and 9.53 electrons/pixel/s with 60 s exposure time. The selected samples were transferred to a 300 kV Titan Krios G3 cryo-TEM microscope (Thermo Fisher Scientific) for imaging. Since wetting the membranes' surface with droplets of water resulted in an uneven distribution of ice on the samples, some areas of the membranes had higher contrast and could be imaged better as they have a thinner ice layer. Thus, we imaged abundant areas with a thin layer of ice where the membrane structures underneath can be clearly resolved. Images were taken at 87,000× magnification, a pixel size of 0.5 nm, and an electron dose of ∼26 electrons/pixel/s (∼1.2 electrons/Å^2/s). Samples were tilted from 60 to −60° in 1° increment (121 images per sample), and the tilt was alternated between positive and negative angles (i.e., 0, −1, 1, −2, 2, −3, 3°,) (i.e., the dose-symmetric tilt scheme) to prevent overexposing of one side of the membrane under the electron beam and the sample damage that would gradually build up during continuous tilt.[94] The exposure time at each angle was ∼4 s, resulting in a total exposure time of ∼500 s. During the tilt series collection, a defocus of ∼3−4 μm was used to enhance the contrast of the features. The eccentricity was maintained automatically by SerialEM software.

Tilt series images were first binned by 4 in the x and y directions to a pixel size of 2 × 2 nm and then reconstructed by IMOD 4.11[60] using the FBP algorithm. Alignment of the tilt series images was achieved by tracking the gold fiducials in each image. The reconstructed tomograms were 4 × 6 μm, and a center area of 2 × 2 μm was cropped for segmentation to avoid reconstruction artifacts (e.g., streaking caused by the missing wedge) near the edge.

Segmentation of the grayscale tomograms was performed in 3D Slicer software. A thresholding and manual correction method was used: for a single slice, a thresholding pixel intensity was set and the image was binarized, followed by manual correction (e.g., painting the edge between the membrane and vacuum/ice, removing artifacts) to account for any errors, as shown in Figure S9. The procedure was repeated for every 10−20 slices, and the complete segmentation was interpolated by the built-in "Grow from seeds" function in 3D Slicer with a seed locality of 0.1. For slices with low contrast (e.g., near the bottom of the membranes, hydrated membranes with poor contrast between the membrane and water), the thresholding and manual correction procedures were performed for each slice without software interpolation. Smoothing filters (opening filter (3 × 3 × 3 pixels) to remove extrusion, median filter (3 × 3 × 3 pixels), and Gaussian filter (2 × 2 × 2 pixels)) were applied to remove artifacts and fuzziness caused by software interpolation.

Volume, Thickness, and Voids Analysis. Quantitative analysis of membrane properties (volume, thickness, etc.) was performed on three reconstructed structures for each membrane type. Only two reconstructions were performed on dry SW30 since only two of the tilt series collected are clear and free of contamination, which were good to reconstruct. The number of membrane voxels was calculated with the built-in "Segmentation statistics" function in 3D Slicer. The volume of the membrane was calculated by multiplying the number of membrane pixels and the size of each voxel (8 nm^3). The polymer fraction of each membrane was generated with the built-in "Segmentation cross-section area" function in 3D Slicer. When comparing two numerical values, we performed a t-test with two independent samples to determine whether the values were significantly different from each other. We defined that the two properties were significantly different when their p values were lower than 0.1 and not different otherwise. For comparisons involving dry SW membranes, only the difference in average numbers was reported and this was specially noted in relevant figure captions.

Effective thickness was calculated from the orthogonal slices of the 3D structures. The reconstructed binary models were first resliced in the y direction in ImageJ to generate the binary orthogonal slices. For each binary slice, the number of membrane pixels in each z-column was

https://doi.org/10.1021/acsnano.5c01190
ACS Nano 2025, 19, 16718−16731

counted and then averaged over the total number of columns (10^6 from a 1000 × 1000 pixels field of view) to obtain the average effective thickness. Columns with no membrane pixels (i.e., through holes caused by reconstruction and segmentation artifacts) were excluded from this calculation. Local thickness of each membrane was calculated in ImageJ with the "Local thickness" plugin.[81] Low-void-fraction layer thickness was defined as the distance between two horizontal slices containing at least 85% membrane materials[33] and was calculated from the polymer fraction data mentioned above.

Enclosed voids were defined as isolated spaces within the membrane structure that are not connected to either the feed or permeate sides. The enclosed voids fraction was calculated using eq 1

$$\text{enclosed void fraction} = \frac{V_{\text{voids}}}{V_{\text{polymer}} + V_{\text{voids}}} \quad (1)$$

where V_{voids} represents the volume of voxels designated as enclosed voids and V_{polymer} represents the volume of voxels designated as membrane material. To identify voids within the membrane structure, we used Amira-Avizo software, version 2023.1 (Thermo Fisher Scientific). We applied the "auto thresholding" method to the segmented binary horizontal slices to select only the "low" voxels with a zero value and obtained the inverted structure (i.e., the structure of open and enclosed voids). Next, the "axis connectivity" option was applied with a neighborhood of 26 (to include voxels sharing at least one common vertex) and z-axis orientation. This step generated a binary image containing all paths connecting the two planes of the image's bounding box. We then subtracted the "connected" voxels (i.e., open voids that connect to the top or bottom) from the inverted structure, resulting with solely the unconnected voxels, which represent the enclosed voids. Various steps were taken to minimize the errors during the calculation of the enclosed void fraction, and details can be found in Section 1.2 in the Supporting Information.

Surface Roughness and Accessible Surface Area Analysis. The roughness of the top surfaces of the membranes was calculated in Omnisurf3D software by using the reconstructed 3D nanostructures. The structures were preprocessed to interpolate missing pixels (i.e., through holes caused by artifacts) in the software, and the pixel with the lowest height was defined as height = 0 nm. The average roughness (R_a) and rms roughness (R_q) was calculated in the software using the preprocessed structures.

Amira-Avizo software was used to calculate the top surface area of the reconstructed 3D structures. We first generated the top and bottom surfaces using the "generate surface" option on the 3D segmented membrane model, which computes a triangular approximation of the interfaces between different materials (e.g., between the membrane and vacuum/water). The sum of the top and bottom surface areas was calculated with the software. The top surface was first cropped away, and the bottom surface area was calculated; the top surface area was then obtained by subtracting the bottom surface area from the sum area. Examples of extracted surfaces can be found in Section 1.3 in the Supporting Information.

ASSOCIATED CONTENT

Supporting Information

The Supporting Information is available free of charge at https://pubs.acs.org/doi/10.1021/acsnano.5c01190.

Movie S1: Beam exposure series of dry SW30 membrane. No bubble formation was observed, indicating no water content in the membrane (AVI)

Movie S2: Beam exposure series of hydrated SW30 membrane. Bubbles were formed under beam damage, indicating the polymer was hydrated and swollen (AVI)

Local polymer connectivity of the hydrated BW membrane (AVI)

Details on QCM measurements of membrane water uptake; examples of extracted membrane top surface features; polymer swelling theories; illustration of the QCM setup; membrane water/vapor uptake results; examples of raw and analyzed QCM data; raw images of the exposure test on hydrated SW and BW membranes; tilt series images and reconstructed sliced without contrast enhancement; examples of segmentation steps; representative top and bottom surfaces of the 3D membrane structures; representative orthogonal slices of 3D membrane structures; polymer fraction graph of SW membranes; local polymer connectivity of SW membranes; examples of enclosed voids isolated from the 3D membrane nanostructures; illustration of the surface probed with AFM and real membrane surface; representative isolated top surface of BW membranes; example features on the isolated top surface; and properties of the membranes that were quantitatively analyzed (PDF)

AUTHOR INFORMATION

Corresponding Authors

Adi M. Ben-Zvi − *Department of Civil & Environmental Engineering, Technion—Israel Institute of Technology, Haifa 32000, Israel; Nanoscience and Nanotechnology Program, Technion—Israel Institute of Technology, Haifa 32000, Israel*; Email: adi-ben-zvi@campus.technion.ac.il

Manish Kumar − *McKetta Department of Chemical Engineering, The University of Texas at Austin, Austin, Texas 78721, United States; Maseeh Department of Civil, Architectural and Environmental Engineering, The University of Texas at Austin, Austin, Texas 78721, United States*; orcid.org/0000-0001-5545-3793; Email: manish.kumar@utexas.edu

Tamar Segal-Peretz − *Department of Chemical Engineering, Technion—Israel Institute of Technology, Haifa 32000, Israel*; orcid.org/0000-0003-3222-6429; Email: tamarps@technion.ac.il

Authors

Chenhao Yao − *McKetta Department of Chemical Engineering, The University of Texas at Austin, Austin, Texas 78721, United States*

Ruizhe Xu − *Maseeh Department of Civil, Architectural and Environmental Engineering, The University of Texas at Austin, Austin, Texas 78721, United States*

Noa Ram − *Department of Chemical Engineering, Technion—Israel Institute of Technology, Haifa 32000, Israel*

Mikhail Stolov − *Department of Chemical Engineering, Technion—Israel Institute of Technology, Haifa 32000, Israel*

Priyanshu Gupta − *McKetta Department of Chemical Engineering, The University of Texas at Austin, Austin, Texas 78721, United States*

Matthew J. Coupin − *Walker Department of Mechanical Engineering, The University of Texas at Austin, Austin, Texas 78712, United States*; orcid.org/0000-0001-6020-1013

Harekrushna Behera − *Maseeh Department of Civil, Architectural and Environmental Engineering, The University of Texas at Austin, Austin, Texas 78721, United States*; orcid.org/0000-0002-8597-5186

Viatcheslav Freger − *Department of Chemical Engineering, Technion—Israel Institute of Technology, Haifa 32000, Israel*; orcid.org/0000-0001-8067-052X

Jamie Warner − *Walker Department of Mechanical Engineering, The University of Texas at Austin, Austin, Texas 78712, United States*; orcid.org/0000-0002-1271-2019

https://doi.org/10.1021/acsnano.5c01190
ACS Nano 2025, 19, 16718−16731

Guy Z. Ramon − *Department of Civil & Environmental Engineering, Technion—Israel Institute of Technology, Haifa 32000, Israel; Nanoscience and Nanotechnology Program and Department of Chemical Engineering, Technion—Israel Institute of Technology, Haifa 32000, Israel;* orcid.org/0000-0002-0711-0654

Complete contact information is available at: https://pubs.acs.org/10.1021/acsnano.5c01190

Author Contributions

¶C.Y. and A.B.-Z. contributed equally to this work.

Notes

The authors declare no competing financial interest.

ACKNOWLEDGMENTS

The authors thank Brilot, A. and Schwartz, E. from the Sauer Structural Biology Laboratory at the University of Texas at Austin for their assistance with tomography data. This work is supported partially through a gift from the WoodNext Foundation and through the use of generous University of Texas Startup funds, partially by the Israel Science Foundation (ISF) grant 3041/21 and the Israel Ministry of Energy grant 222-11-088, and partially by National Alliance for Water Innovation (NAWI) funded by the U.S. Department of Energy, Office of Energy Efficiency and Renewable Energy (EERE), Advanced Manufacturing Office, under Funding Opportunity Announcement Number DE-FOA-0001905. AB was supported, in part, by the Jewish National Fund (JNF)'s "climate" fellowship. The collaboration between Technion and UT Austin was supported by a Binational Science Foundation (BSF) Rahamimoff travel grant.

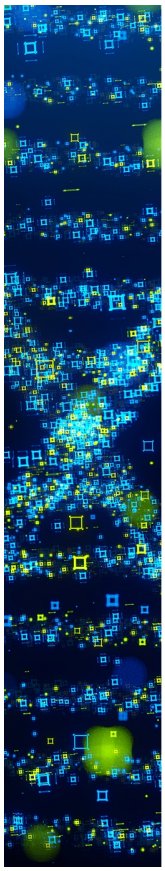
REFERENCES

(1) Elimelech, M.; Phillip, W. A. The Future of Seawater Desalination: Energy, Technology, and the Environment. *Science* **2011**, *333*, 712−717.
(2) Fritzmann, C.; Löwenberg, J.; Wintgens, T.; Melin, T. State-of-the-Art of Reverse Osmosis Desalination. *Desalination* **2007**, *216*, 1−76.
(3) Kurihara, M.; Sasaki, T.; Swro, L. The Pursuits of Ultimate Membrane Technology Including Low Pressure Seawater Reverse Osmosis Membrane Developed by "Mega-Ton Water System" Project. *J. Membr. Sci. Res.* **2017**, *3*, 157−173.
(4) Wang, L.; He, J.; Heiranian, M.; Fan, H.; Song, L.; Li, Y.; Elimelech, M. Water Transport in Reverse Osmosis Membranes Is Governed by Pore Flow, Not a Solution-Diffusion Mechanism. *Sci. Adv.* **2023**, *9*, No. eadf8488.
(5) Petersen, R. J. Composite Reverse Osmosis and Nanofiltration Membranes. *J. Membr. Sci.* **1993**, *83*, 81−150.
(6) Lee, K. P.; Arnot, T. C.; Mattia, D. A Review of Reverse Osmosis Membrane Materials for Desalination—Development to Date and Future Potential. *J. Membr. Sci.* **2011**, *370*, 1−22.
(7) Tan, Z.; Chen, S.; Peng, X.; Zhang, L.; Gao, C. Polyamide Membranes with Nanoscale Turing Structures for Water Purification. *Science* **2018**, *360*, 518−521.
(8) Marchetti, P.; Jimenez Solomon, M. F.; Szekely, G.; Livingston, A. G. Molecular Separation with Organic Solvent Nanofiltration: A Critical Review. *Chem. Rev.* **2014**, *114*, 10735−10806.
(9) Thompson, K. A.; Mathias, R.; Kim, D.; Kim, J.; Rangnekar, N.; Johnson, J. R.; Hoy, S. J.; Bechis, I.; Tarzia, A.; Jelfs, K. E.; McCool, B. A.; Livingston, A. G.; Lively, R. P.; Finn, M. G. N-Aryl-Linked Spirocyclic Polymers for Membrane Separations of Complex Hydrocarbon Mixtures. *Science* **2020**, *369*, 310−315.
(10) Poloncarzova, M.; Vejrazka, J.; Vesely, V.; Izak, P. Biogas Purification Effective Purification of Biogas by a Condensing-Liquid Membrane. *Angew. Chem., Int. Ed.* **2011**, *50*, 669−671.
(11) Cadotte, J. E.; Petersen, R. J.; Larson, R. E.; Erickson, E. E. A New Thin-Film Composite Seawater Reverse Osmosis Membrane. *Desalination* **1980**, *32*, 25−31.
(12) McCutcheon, J. R. Unraveling the Mysteries of the Thin Film Composite Reverse Osmosis Membrane. *Joule* **2021**, *5*, 528−530.
(13) Cadotte, J. E. Interfacially synthesized reverse osmosis membrane U.S. Patent 4,277,344 A, 1981.
(14) Habib, S.; Weinman, S. T. A Review on the Synthesis of Fully Aromatic Polyamide Reverse Osmosis Membranes. *Desalination* **2021**, *502*, 114939.
(15) Geise, G. M.; Paul, D. R.; Freeman, B. D. Fundamental Water and Salt Transport Properties of Polymeric Materials. *Prog. Polym. Sci.* **2014**, *39*, 1−42.
(16) Nunes, S. P.; Culfaz-Emecen, P. Z.; Ramon, G. Z.; Visser, T.; Koops, G. H.; Jin, W.; Ulbricht, M. Thinking the Future of Membranes: Perspectives for Advanced and New Membrane Materials and Manufacturing Processes. *J. Membr. Sci.* **2020**, *598*, 117761.
(17) Lin, L.; Lopez, R.; Ramon, G. Z.; Coronell, O. Investigating the Void Structure of the Polyamide Active Layers of Thin-Film Composite Membranes. *J. Membr. Sci.* **2016**, *497*, 365−376.
(18) Ukrainsky, B.; Ramon, G. Z. Temperature Measurement of the Reaction Zone during Polyamide Film Formation by Interfacial Polymerization. *J. Membr. Sci.* **2018**, *566*, 329−335.
(19) Stolov, M.; Freger, V. Membrane Charge Weakly Affects Ion Transport in Reverse Osmosis. *Environ. Sci. Technol. Lett.* **2020**, *7*, 440−445.
(20) Wong, M. C. Y.; Lin, L.; Coronell, O.; Hoek, E. M. V.; Ramon, G. Z. Impact of Liquid-Filled Voids within the Active Layer on Transport through Thin-Film Composite Membranes. *J. Membr. Sci.* **2016**, *500*, 124−135.
(21) Mondal, S.; Griffiths, I. M.; Ramon, G. Z. Forefronts in Structure−Performance Models of Separation Membranes. *J. Membr. Sci.* **2019**, *588*, 117166.
(22) Nulens, I.; Ben Zvi, A.; Vankelecom, I. F. J.; Ramon, G. Z. Re-Thinking Polyamide Thin Film Formation: How Does Interfacial Destabilization Dictate Film Morphology? *J. Membr. Sci.* **2022**, *656*, 120593.
(23) Cui, Y.; Liu, X. Y.; Chung, T. S. Ultrathin Polyamide Membranes Fabricated from Free-Standing Interfacial Polymerization: Synthesis, Modifications, and Post-Treatment. *Ind. Eng. Chem. Res.* **2017**, *56*, 513−523.
(24) Ali, Z.; Al Sunbul, Y.; Pacheco, F.; Ogieglo, W.; Wang, Y.; Genduso, G.; Pinnau, I. Defect-Free Highly Selective Polyamide Thin-Film Composite Membranes for Desalination and Boron Removal. *J. Membr. Sci.* **2019**, *578*, 85−94.
(25) Khorshidi, B.; Thundat, T.; Fleck, B. A.; Sadrzadeh, M. Thin Film Composite Polyamide Membranes: Parametric Study on the Influence of Synthesis Conditions. *RSC Adv.* **2015**, *5*, 54985−54997.
(26) Park, S. H.; Kwon, S. J.; Shin, M. G.; Park, M. S.; Lee, J. S.; Park, C. H.; Park, H.; Lee, J. H. Polyethylene-Supported High Performance Reverse Osmosis Membranes with Enhanced Mechanical and Chemical Durability. *Desalination* **2018**, *436*, 28−38.
(27) Roh, I. J.; Greenberg, A. R.; Khare, V. P. Synthesis and Characterization of Interfacially Polymerized Polyamide Thin Films. *Desalination* **2006**, *191*, 279−290.
(28) Xu, J.; Yan, H.; Zhang, Y.; Pan, G.; Liu, Y. The Morphology of Fully-Aromatic Polyamide Separation Layer and Its Relationship with Separation Performance of TFC Membranes. *J. Membr. Sci.* **2017**, *541*, 174−188.
(29) Culp, T. E.; Khara, B.; Brickey, K. P.; Geitner, M.; Zimudzi, T. J.; Wilbur, J. D.; Jons, S. D.; Roy, A.; Paul, M.; Ganapathysubramanian, B.; Zydney, A. L.; Kumar, M.; Gomez, E. D. Nanoscale Control of Internal Inhomogeneity Enhances Water Transport in Desalination Membranes. *Science* **2021**, *371*, 72−75.

(30) Pacheco, F.; Sougrat, R.; Reinhard, M.; Leckie, J. O.; Pinnau, I. 3D Visualization of the Internal Nanostructure of Polyamide Thin Films in RO Membranes. *J. Membr. Sci.* **2016**, *501*, 33−44.
(31) Culp, T. E.; Shen, Y.; Geitner, M.; Paul, M.; Roy, A.; Behr, M. J.; Rosenberg, S.; Gu, J.; Kumar, M.; Gomez, E. D. Electron Tomography Reveals Details of the Internal Microstructure of Desalination Membranes. *Proc. Natl. Acad. Sci. U.S.A.* **2018**, *115*, 8694−8699.
(32) An, H.; Smith, J. W.; Ji, B.; Cotty, S.; Zhou, S.; Yao, L.; Kalutantirige, F. C.; Chen, W.; Ou, Z.; Su, X.; Feng, J.; Chen, Q. Mechanism and Performance Relevance of Nanomorphogenesis in Polyamide Films Revealed by Quantitative 3D Imaging and Machine Learning. *Sci. Adv.* **2022**, *8*, No. eabk1888.
(33) Li, D.; Lu, R.; Wang, K.; Li, Y.; Lin, W.; Wang, X.; Shen, Y.; Huang, X. Neural Network-Assisted Data Processing Improved Tomography Characterizations of Reverse Osmosis Polyamide Layers. *ACS ES&T Eng.* **2024**, *4*, 128−138.
(34) Kłosowski, M. M.; McGilvery, C. M.; Li, Y.; Abellan, P.; Ramasse, Q.; Cabral, J. T.; Livingston, A. G.; Porter, A. E. Micro-to Nano-Scale Characterisation of Polyamide Structures of the SW30HR RO Membrane Using Advanced Electron Microscopy and Stain Tracers. *J. Membr. Sci.* **2016**, *520*, 465−476.
(35) Yao, L.; An, H.; Zhou, S.; Kim, A.; Luijten, E.; Chen, Q. Seeking Regularity from Irregularity: Unveiling the Synthesis-Nanomorphology Relationships of Heterogeneous Nanomaterials Using Unsupervised Machine Learning. *Nanoscale* **2022**, *14*, 16479−16489.
(36) Song, X.; Smith, J. W.; Kim, J.; Zaluzec, N. J.; Chen, W.; An, H.; Dennison, J. M.; Cahill, D. G.; Kulzick, M. A.; Chen, Q. Unraveling the Morphology−Function Relationships of Polyamide Membranes Using Quantitative Electron Tomography. *ACS Appl. Mater. Interfaces* **2019**, *11*, 8517−8526.
(37) Li, Y.; Kłosowski, M. M.; McGilvery, C. M.; Porter, A. E.; Livingston, A. G.; Cabral, J. T. Probing Flow Activity in Polyamide Layer of Reverse Osmosis Membrane with Nanoparticle Tracers. *J. Membr. Sci.* **2017**, *534*, 9−17.
(38) Freger, V. Swelling and Morphology of the Skin Layer of Polyamide Composite Membranes: An Atomic Force Microscopy Study. *Environ. Sci. Technol.* **2004**, *38*, 3168−3175.
(39) Dražević, E.; Košutić, K.; Freger, V. Permeability and Selectivity of Reverse Osmosis Membranes: Correlation to Swelling Revisited. *Water Res.* **2014**, *49*, 444−452.
(40) Lee, J.; Doherty, C. M.; Hill, A. J.; Kentish, S. E. Water Vapor Sorption and Free Volume in the Aromatic Polyamide Layer of Reverse Osmosis Membranes. *J. Membr. Sci.* **2013**, *425*−*426*, 217−226.
(41) Zhang, W.; Qin, Y.; Shi, W.; Hu, Y. Unveiling the Molecular Mechanisms of Thickness-Dependent Water Dynamics in an Ultrathin Free-Standing Polyamide Membrane. *J. Phys. Chem. B* **2020**, *124*, 11939−11948.
(42) Freger, V.; Ramon, G. Z. Polyamide Desalination Membranes: Formation, Structure, and Properties. *Prog. Polym. Sci.* **2021**, *122*, 101451.
(43) Auer, M. Three-Dimensional Electron Cryo-Microscopy as a Powerful Structural Tool in Molecular Medicine. *J. Mol. Med.* **2000**, *78*, 191−202.
(44) Bodakuntla, S.; Kuhn, C. C.; Biertümpfel, C.; Mizuno, N. Cryo-Electron Microscopy in the Fight against COVID-19—Mechanism of Virus Entry. *Front. Mol. Biosci.* **2023**, *10*, 1252529.
(45) Gan, L.; Jensen, G. J. Electron Tomography of Cells. *Q. Rev. Biophys.* **2012**, *45*, 27−56.
(46) Stewart, P. L. Cryo-electron Microscopy and Cryo-electron Tomography of Nanoparticles. *Wiley Interdiscip. Rev. Nanomed. Nanobiotechnol.* **2017**, *9*, No. e1417.
(47) Tian, Y.; Wang, T.; Liu, W.; Xin, H. L.; Li, H.; Ke, Y.; Shih, W. M.; Gang, O. Prescribed Nanoparticle Cluster Architectures and Low-Dimensional Arrays Built Using Octahedral DNA Origami Frames. *Nat. Nanotechnol.* **2015**, *10*, 637−644.
(48) Ghasemi, M.; Geitner, M.; O'connell, A.; Gomez, E. D. Three-Dimensional Morphology of Polymeric Membranes from Electron Tomography. *Annu. Rev. Chem. Biomol. Eng.* **2024**, *15*, 219−241.
(49) Chen, X. C.; Jiang, X.; Balsara, N. P. Swelling of Individual Nanodomains in Hydrated Block Copolymer Electrolyte Membranes. *J. Chem. Phys.* **2018**, *149*, 163325.
(50) Jiang, X.; Sun, J.; Zuckermann, R. N.; Balsara, N. P. Effect of Hydration on Morphology of Thin Phosphonate Block Copolymer Electrolyte Membranes Studied by Electron Tomography. *Polym. Eng. Sci.* **2021**, *61*, 1104−1115.
(51) Allen, F. I.; Comolli, L. R.; Kusoglu, A.; Modestino, M. A.; Minor, A. M.; Weber, A. Z. Morphology of Hydrated As-Cast Nafion Revealed through Cryo Electron Tomography. *ACS Macro Lett.* **2015**, *4*, 1−5.
(52) Song, W.; Park, J.; Dasgupta, S.; Yao, C.; Maroli, N.; Behera, H.; Yin, X.; Acharya, D. P.; Zhang, X.; Doherty, C. M.; Maiti, P. K.; Freeman, B. D.; Kumar, M. Scalable Pillar[5]Arene-Integrated Poly(Arylate-Amide) Molecular Sieve Membranes to Separate Light Gases. *Chem. Mater.* **2022**, *34*, 6559−6567.
(53) Baker, L. A.; Rubinstein, J. L. Radiation Damage in Electron Cryomicroscopy. *Methods Enzymol.* **2010**, *481*, 371−388.
(54) Fahy, G. M.; Wowk, B. Principles of Cryopreservation by Vitrification. *Methods Mol. Biol.* **2015**, *1257*, 21−82.
(55) Dubochet, J.; Adrian, M.; Chang, J.-J.; Homo, J.-C.; Lepault, J.; McDowall, A. W.; Schultz, P. Cryo-Electron Microscopy of Vitrified Specimens. *Q. Rev. Biophys.* **1988**, *21*, 129−228.
(56) Benjin, X.; Ling, L. Developments, Applications, and Prospects of Cryo-electron Microscopy. *Protein Sci.* **2020**, *29*, 872−882.
(57) Milne, J. L. S.; Borgnia, M. J.; Bartesaghi, A.; Tran, E. E. H.; Earl, L. A.; Schauder, D. M.; Lengyel, J.; Pierson, J.; Patwardhan, A.; Subramaniam, S. Cryo-electron Microscopy − a Primer for the Non-microscopist. *FEBS J.* **2013**, *280*, 28−45.
(58) Stossi, F.; Singh, P. K. Basic Image Analysis and Manipulation in ImageJ/Fiji. *Curr. Protoc. Mol. Biol.* **2023**, *3*, No. e849.
(59) Wade, R. H. A Brief Look at Imaging and Contrast Transfer. *Ultramicroscopy* **1992**, *46*, 145−156.
(60) Mastronarde, D. N.; Held, S. R. Automated Tilt Series Alignment and Tomographic Reconstruction in IMOD. *J. Struct. Biol.* **2017**, *197*, 102−113.
(61) Arslan, I.; Tong, J. R.; Midgley, P. A. Reducing the Missing Wedge: High-Resolution Dual Axis Tomography of Inorganic Materials. *Ultramicroscopy* **2006**, *106*, 994−1000.
(62) Midgley, P. A.; Weyland, M. 3D Electron Microscopy in the Physical Sciences: The Development of Z-Contrast and EFTEM Tomography. *Ultramicroscopy* **2003**, *96*, 413−431.
(63) Cadotte, J. E.; Peterson, R. J.; Turbak, A. F. Thin-Film Composite Reverse-Osmosis Membranes: Origin, Development, and Recent Advances. In *Synthetic Membranes*; ACS, 1981; pp 305−326.
(64) Kalutantirige, F. C.; He, J.; Yao, L.; Cotty, S.; Zhou, S.; Smith, J. W.; Tajkhorshid, E.; Schroeder, C. M.; Moore, J. S.; An, H.; Su, X.; Li, Y.; Chen, Q. Beyond Nothingness in the Formation and Functional Relevance of Voids in Polymer Films. *Nat. Commun.* **2024**, *15*, 2852.
(65) Yang, Z.; Guo, H.; Tang, C. Y. The Upper Bound of Thin-Film Composite (TFC) Polyamide Membranes for Desalination. *J. Membr. Sci.* **2019**, *590*, 117297.
(66) Lim, Y. J.; Goh, K.; Kurihara, M.; Wang, R. Seawater Desalination by Reverse Osmosis: Current Development and Future Challenges in Membrane Fabrication − A Review. *J. Membr. Sci.* **2021**, *629*, 119292.
(67) Geise, G. M.; Park, H. B.; Sagle, A. C.; Freeman, B. D.; McGrath, J. E. Water Permeability and Water/Salt Selectivity Tradeoff in Polymers for Desalination. *J. Membr. Sci.* **2011**, *369*, 130−138.
(68) Puffr, R.; Šebenda, J. On the Structure and Properties of Polyamides. XXVII. The Mechanism of Water Sorption in Polyamides. *J. Polym. Sci., Part C* **1967**, *16*, 79−93.
(69) Flory, P. J.; Rehner, J. Statistical Mechanics of Cross-Linked Polymer Networks II. Swelling. *J. Chem. Phys.* **1943**, *11*, 521−526.
(70) Chan, E. P.; Young, A. P.; Lee, J.; Chung, J. Y.; Stafford, C. M. Swelling of Ultrathin Crosslinked Polyamide Water Desalination Membranes. *J. Polym. Sci., Part B:Polym. Phys.* **2013**, *51*, 385−391.
(71) Chan, E. P.; Young, A. P.; Lee, J.; Stafford, C. M. Swelling of Ultrathin Molecular Layer-by-Layer Polyamide Water Desalination Membranes. *J. Polym. Sci., Part B:Polym. Phys.* **2013**, *51*, 1647−1655.

https://doi.org/10.1021/acsnano.5c01190
ACS Nano 2025, 19, 16718−16731

(72) Nadermann, N. K.; Chan, E. P.; Stafford, C. M. Bilayer Mass Transport Model for Determining Swelling and Diffusion in Coated, Ultrathin Membranes. *ACS Appl. Mater. Interfaces* **2015**, *7*, 3492−3502.
(73) Fan, H.; Elimelech, M.; Biesheuvel, P. M. Theory of Expansion and Compression of Polymeric Materials: Implications for Membrane Solvent Flow under Compaction. *J. Membr. Sci.* **2024**, *697*, 122576.
(74) Zhu, Y.; Gui, L.; Wang, R.; Wang, Y.; Fang, W.; Elimelech, M.; Lin, S.; Jin, J. Regulation of Molecular Transport in Polymer Membranes with Voltage-Controlled Pore Size at the Angstrom Scale. *Nat. Commun.* **2023**, *14*, 2373.
(75) McKenna, G. B.; Flynn, K. M.; Chen, Y. Swelling in Crosslinked Natural Rubber: Experimental Evidence of the Crosslink Density Dependence of χ. *Polymer* **1990**, *31*, 1937−1945.
(76) Orski, S. V.; Page, K. A.; Chan, E. P.; Beers, K. L.; Horkay, F.; Douglas, J. F.; Del Gado, E. Model Polymer Thin Films to Measure Structure and Dynamics of Confined, Swollen Networks. In *Gels and Other Soft Amorphous Solids*; ACS, 2018; pp 91−115.
(77) McCrackin, F. L.; Passaglia, E.; Stromberg, R. R.; Steinberg, H. L. Measurement of the Thickness and Refractive Index of Very Thin Films and the Optical Properties of Surfaces by Ellipsometry. *J. Res. Natl. Bur. Stand., Sect. A* **1963**, *67*, 363.
(78) Freger, V. Nanoscale Heterogeneity of Polyamide Membranes Formed by Interfacial Polymerization. *Langmuir* **2003**, *19*, 4791−4797.
(79) Lin, L.; Feng, C.; Lopez, R.; Coronell, O. Identifying Facile and Accurate Methods to Measure the Thickness of the Active Layers of Thin-Film Composite Membranes − A Comparison of Seven Characterization Techniques. *J. Membr. Sci.* **2016**, *498*, 167−179.
(80) Hildebrand, T.; Rüegsegger, P. A New Method for the Model-independent Assessment of Thickness in Three-dimensional Images. *J. Microsc.* **1997**, *185*, 67−75.
(81) Dougherty, R.; Kunzelmann, K.-H. Computing Local Thickness of 3D Structures with ImageJ. *Microsc. Microanal.* **2007**, *13*, 1678−1679.
(82) Ma, X.-H.; Yao, Z.-K.; Yang, Z.; Guo, H.; Xu, Z.-L.; Tang, C. Y.; Elimelech, M. Nanofoaming of Polyamide Desalination Membranes to Tune Permeability and Selectivity. *Environ. Sci. Technol. Lett.* **2018**, *5*, 123−130.
(83) Kolev, V.; Freger, V. Hydration, Porosity and Water Dynamics in the Polyamide Layer of Reverse Osmosis Membranes: A Molecular Dynamics Study. *Polymer* **2014**, *55*, 1420−1426.
(84) Ma, X.; Yang, Z.; Yao, Z.; Guo, H.; Xu, Z.; Tang, C. Y. Tuning Roughness Features of Thin Film Composite Polyamide Membranes for Simultaneously Enhanced Permeability, Selectivity and Anti-Fouling Performance. *J. Colloid Interface Sci.* **2019**, *540*, 382−388.
(85) Mahlangu, O. T.; Nthunya, L. N.; Motsa, M. M.; Morifi, E.; Richards, H.; Mamba, B. B. Fouling of High Pressure-Driven NF and RO Membranes in Desalination Processes: Mechanisms and Implications on Salt Rejection. *Chem. Eng. Res. Des.* **2023**, *199*, 268−295.
(86) Vrijenhoek, E. M.; Hong, S.; Elimelech, M. Influence of Membrane Surface Properties on Initial Rate of Colloidal Fouling of Reverse Osmosis and Nanofiltration Membranes. *J. Membr. Sci.* **2001**, *188*, 115−128.
(87) Rahaman, Md. S.; Thérien-Aubin, H.; Ben-Sasson, M.; Ober, C. K.; Nielsen, M.; Elimelech, M. Control of Biofouling on Reverse Osmosis Polyamide Membranes Modified with Biocidal Nanoparticles and Antifouling Polymer Brushes. *J. Mater. Chem. B* **2014**, *2*, 1724.
(88) Lowell, S.; Shields, J. E.; Thomas, M. A.; Thommes, M. *Characterization of Porous Solids and Powders: Surface Area, Pore Size and Density*; Springer Netherlands: Dordrecht, 2004; Vol. *16*.
(89) Ramon, G. Z.; Hoek, E. M. V. Transport through Composite Membranes, Part 2: Impacts of Roughness on Permeability and Fouling. *J. Membr. Sci.* **2013**, *425−426*, 141−148.
(90) Thomas, J.; Ramm, J.; Gemming, T. Density Measurement of Thin Layers by Electron Energy Loss Spectroscopy (EELS). *Micron* **2013**, *50*, 57−61.
(91) Louf, J.-F.; Lu, N. B.; O'Connell, M. G.; Cho, H. J.; Datta, S. S. Under Pressure: Hydrogel Swelling in a Granular Medium. *Sci. Adv.* **2021**, *7*, No. eabd2711.
(92) Lietor-Santos, J.-J.; Sierra-Martin, B.; Vavrin, R.; Hu, Z.; Gasser, U.; Fernandez-Nieves, A. Deswelling Microgel Particles Using Hydrostatic Pressure. *Macromolecules* **2009**, *42*, 6225−6230.
(93) Tarnapolsky, A.; Freger, V. Modeling QCM-D Response to Deposition and Attachment of Microparticles and Living Cells. *Anal. Chem.* **2018**, *90*, 13960−13968.
(94) Hagen, W. J. H.; Wan, W.; Briggs, J. A. G. Implementation of a Cryo-Electron Tomography Tilt-Scheme Optimized for High Resolution Subtomogram Averaging. *J. Struct. Biol.* **2017**, *197*, 191−198.


CAS BIOFINDER DISCOVERY PLATFORM™
STOP DIGGING THROUGH DATA —START MAKING DISCOVERIES
CAS BioFinder helps you find the right biological insights in seconds
Start your search
CAS
A division of the American Chemical Society

https://doi.org/10.1021/acsnano.5c01190
ACS Nano 2025, 19, 16718−16731